Environmental Science
Processes & Impacts

Accepted Manuscript

This article can be cited before page numbers have been issued, to do this please use: A. Roy, D. CHEN, A. Bogush and J. Stegemann, *Environ. Sci.: Processes Impacts*, 2026, DOI: 10.1039/D5EM00651A.

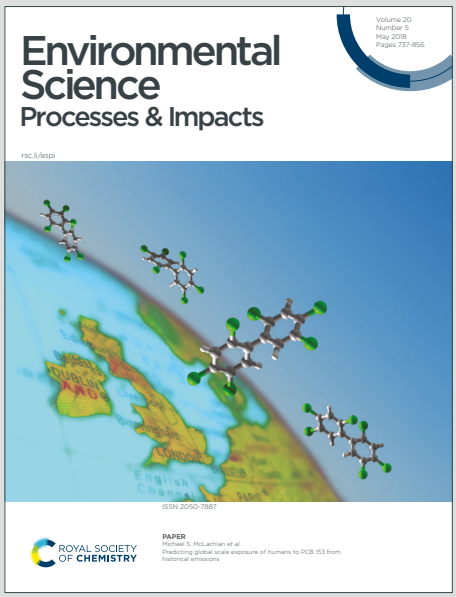

View Article Online
DOI: 10.1039/D5EM00651A

Environmental Significance Statement

WSAir pollution control residues (APCRs) from waste-to-energy plants are hazardous wastes due to their high alkalinity and toxic element contents that are difficult to recover or treat for disposal. Industrial treatment with acid wastes neutralises their corrosivity before landfilling, but the common perception that this changes zinc speciation and leachability is unevidenced. Using advanced XAS and leaching tests, our results show that zinc occurs mainly as spinel, hemimorphite, glassy phases, zinc phosphate and hydrozincite in APCRs, and these species persist after acid neutralisation, which does not alter their fundamental leachability. The evidence challenges the effectiveness of current practices and underscores the urgent need for a more sustainable approach to management of APCRs.

SPECIATION AND LEACHABILITY OF ZINC IN ENERGY-FROM-WASTE AIR POLLUTION CONTROL RESIDUES AND EFFECTS OF PARTIAL NEUTRALISATION

View Article Online
DOI: 10.1039/D5EM00651A

Amitava Roy[1], Dan Ting Chen[2], Anna Bogush[2] and Julia A. Stegemann[2*]

ABSTRACT

Seven UK air pollution control residues (APCR) from municipal solid waste combustion were examined to understand the speciation of potentially ecotoxic zinc, before and after partial APCR neutralisation using acid wastes, as is sometimes conducted before disposal. Fe K-edge XAS showed Zn-containing magnetite (spinel) is an important phase in APCR, along with ferrihydrite. Linear combination fitting of X-ray absorption near edge structure (XANES) Zn K-edge spectra strongly concluded that the 2600-7300 mg/kg of zinc in the APCR is speciated mainly as spinel, hemimorphite, a glassy phase, zinc phosphate and hydrozincite, with statistically consistent findings both within and between APCRs. The extended X-ray absorption fine structure (EXAFS) spectra of the APCR mainly show the first Zn-O shell which is consistent with Zn in solid solution, glass and poorly crystalline phases. Presented in the context of a full review of previous studies, these results suggest changes in Zn speciation under modern operating regimes. pH-dependent leaching behaviour of the raw APCRs was consistent with solubility control by secondary $Zn(OH)_2$ over the alkaline range, and also $Zn_5(OH)_8Cl$ and hydrozincite at mid-alkaline pH. Partial neutralisation of the APCRs with concentrated HCl formed secondary reaction products that agglomerated the APCRs, but the same zinc species were found after neutralisation, and lower zinc leachability is attributable only to decreasing the pH to 10.0-10.7. Since this pH is unlikely to be stable in the environment (e.g., in interaction with landfill leachate at pH 5-8), industrial "treatment" by partial neutralisation does not reduce the environmental risk associated with zinc in APCRs.

KEYWORDS

fly ash, municipal solid waste incinerator ash, MSWI, waste-to-energy, WtE, solubility, environmental impact

[1]*Centre for Advanced Microstructures & Devices, Louisiana State University, 6980 Jefferson Hwy, Baton Rouge LA 70806, USA*
[2]*Centre for Resource Efficiency & the Environment (CREE), Department of Civil, Environmental & Geomatic Engineering (CEGE), University College London (UCL), Chadwick Building, Gower Street, London WC1E 6BT, UK*
**Corresponding Author, Phone: +44(0)207 679 7370. E-mail: j.stegemann@ucl.ac.uk (J. A. Stegemann)*

View Article Online
DOI: 10.1039/D5EM00651A

1 INTRODUCTION

Generation of energy from waste (EfW) is a common way to recover value from municipal solid waste (MSW). Air pollution control residues (APCR) from MSW combustion represent only 2 to 6% of the original volume of the MSW. However, they are classified as hazardous waste in most jurisdictions (e.g., under European List of Wastes code 19 01 07*; European Commission Decision 2000/532/EC) as they are alkaline (corrosive) and contain high concentrations of toxic metals, such as zinc and lead, and soluble anions, such as chlorides and sulphates, and are difficult to recover or treat for disposal. One approach that has been applied industrially in the United Kingdom (UK) and elsewhere, is addition of acid wastes to APCRs and blending with other neutralised wastes before landfilling. The main purpose of this treatment is to neutralise the corrosivity hazard but there is also an unevidenced conception that the agglomeration resulting from this treatment changes zinc speciation and leachability. The work reported here used X-ray absorption spectroscopy (XAS), a powerful technique for direct molecular-level study of specific elements at relatively low concentrations in complex materials, irrespective of their crystallinity, and pH-dependent leaching to gain a better understanding of the zinc speciation in, and leachability from, APCR, before and after partial neutralisation.

2 PREVIOUS WORK

APCR from MSW combustion are generated in the flue gas cleaning process, and comprise fly ash particles and scrubbing residues, often with excess hydrated lime ($Ca(OH)_2$). The overall composition and mineralogy of APCRs is fundamental to zinc speciation and has been addressed in a previous publication[1].

The concentration and speciation of zinc in APCR depends on the type of waste combusted, its content of chlorine, sulphur and water, the amount of excess air, and temperatures and residence times in the various stages of combustion and pollution control. Theoretically, zinc present in MSW as a metal or oxide should be completely volatilised during combustion and deposited on the surface of fly ash particles as a chloride, and/or an oxide[1], but in practice it tends to partition approximately equally between the APCR and the bottom ash[2]. This partitioning may result from reaction of zinc to form less volatile Zn_2SiO_4 and $ZnAl_2O_4$ [3] at MSW combustion flame temperatures (≈1200°C)[4]. Zn in APCR has been shown to be more concentrated with unreacted lime in the smallest size fraction[5]. Specific minerals previously identified for zinc in MSW fly ash and APCR by instrumental methods and geochemical equilibrium modelling are shown in Table 1. Zinc chlorides, hydrated chlorides and oxides dominate previous findings, but most workers have suggested that contaminants, including zinc, are widely dispersed in the APCR, with various types of uptake by a variety of minerals and also glass. The only other previous XAS investigation of APCRs found that K_2ZnCl_4 predominated, with the presence of hemimorphite ($Zn_4Si_2O_7(OH)_2 \cdot H_2O$, spinels ($ZnFe_2O_4$, $ZnAl_2O_4$), surface adsorbed zinc, and hydrozincite ($Zn_5(CO_3)_2(OH)_6$)[6].

The controlling mineral phases previously identified for zinc leachability above pH 7 have been shown in bold characters in Table 1. Zinc oxide and hydroxide were shown to control zinc concentrations in solution in the alkaline pH range typical of water leachates of APCR, though Eighmy, *et al.*[7] did conclude that leaching of zinc was controlled by $ZnCO_3$, and Astrup, *et al.*[8] and Wang, *et al.*[9] also found Zn_2SiO_4 to control zinc leaching for some APCR. Interestingly, Zhang, *et al.*[10] found control of leaching in the neutral range by a zinc hydroxychloride, $Zn_5(OH)_8Cl_2$, though ZnO dominated at higher pH.

Table 1. Zinc mineral phases previously identified in fly ash (*) and APCRs (+) from combustion of municipal solid waste

Source	Zinc oxide (including zincite) ZnO	Zinc hydroxide $Zn(OH)_2$	Calcium zincate $CaZn_2(OH)_6 \cdot 2H_2O$	Hydrozincite $Zn_5(CO_3)_2(OH)_6 \cdot x H_2O$	Smithsonite $ZnCO_3$	Zinc chloride $ZnCl_2$	Simonkolleite $Zn_5(OH)_8Cl_2$	Potassium tetrachlorozincate K_2ZnCl_4	Zinc bromide $ZnBr_2$	Gordaite $Zn_4Na(OH)_6(SO_4)Cl \cdot 6\ H_2O$	Zinc oxiysulphate $Zn_3O(SO_4)_2$	Zinc sulphate $ZnSO_4 \cdot xH_2O$	Wurtzite / sphalerite ZnS	Zincowoodwardite $Al_{0.375}H_6O^{2.686}S_{0.18}{}_8Zn_{0.625}$	Spinel $(Zn, Ni, Fe)Fe_2O_4$	Gahnite $ZnAl_2O_4$	Zinc phosphate $(Zn_3(PO_4)_2)$	Hemimorphite $Zn_4Si_2O_7(OH)_2 \cdot 2H_2O$	Willemite Zn_2SiO_4	Zinc silicate $ZnSiO_3$	Zinc metal Zn
a*	X				**W**	X		X	X		X	W						X		W	X
b						X*									X*						X*+
c*	X																				
d*							X						X			X			X		
e	X+					X*+							X*+		X*+	X*					
f+	**W**		**W**																**W**	W	
g+	**W**						**W**														
h+	**W**	**W**																	**W**		
i+	X					X															X
j+				X		X						X									
k*	W							X		W			X								
l+																		X	X		
m+	**W**																		**W**		
n+	X					X					X										
o				X*+				X*+							X*+		X*+				

X indicates phase identified in unaltered APCR; W indicates phase identified in hydrated APCR

a [7], b [11], c [12], d [13], e [14], f [8], g [10], h [15], I [16], j [17], k [18], l [19], m [9], n [20], o [6]

View Article Online
DOI: 10.1039/D5EM00651A

Struis, *et al.*[13] found gahnite ($ZnAlO_4$) to be an important Zn containing phase in a Swiss MSW fly ash, and Rissler, *et al.*[6], Rissler, *et al.*[21] additionally found franklinite, with more of both spinels in APCRs from fluidised bed facilities than fly ash from grate combustion systems, in Sweden. Spinels have the general formula $A^{2+}B^{3+}{}_2\Theta_4$ (mostly cubic crystal structure), where the (tetrahedral) A site is usually occupied by divalent elements, such as Mg^{2+}, Fe^{2+}, Zn^{2+}, the (octahedral) B site is usually occupied by trivalent elements, such as Al^{3+}, Cr^{3+}, Fe^{3+}, and Θ can be O, S, Se, or similar anions[22]. There is extensive solid solution among the end members franklinite and gahnite at high temperatures, but immiscibility exists at lower temperatures[23, 24]. The most common spinel is magnetite, $Fe^{2+}Fe^{3+}{}_2O_4$, which is found in many rocks and industrial by-products. Wei, *et al.*[25] reported magnetite, with various levels of substitution by Al and Ti, as an important phase in a MSW incineration bottom ash from Japan. Magnetite is found in fly ashes from coal-fired power plants, where it is mostly produced by the breakdown of pyrite in the coal during its firing[26, 27]. Gomes, *et al.*[28] found that the magnetite in coal fly ash has a complex composition, with Mg^{2+} replacing Fe^{2+} and containing other minor elements such as Si. Magnetite is also found in other residues from thermal processing, including electric arc furnace dust[29, 30] and non-ferrous smelter slags[31]. Manceau, *et al.*[32] found that Zn-containing magnetite is an important component of the contaminated soil around some historical smelters in France. As the spinel phase can be an important repository of zinc, special emphasis is placed on the magnetic fraction of APCRs in this investigation.

3 MATERIALS & METHODS

3.1 Air Pollution Control Residues

Seven APCR samples from six different UK EfW facilities, characterised in previous work[1], were used in the work reported here. The samples are identified as A3 and A8 (both from the same source but sampled at different times), 1, 2, 4, 5, and 9. The concentration of zinc in these APCR samples ranged from 0.26 to 0.73%; average concentrations of major matrix elements determined by inductively coupled plasma optical emission or mass spectroscopy following aqua regia digestion are shown in Table 2.

Table 2. Average major element concentrations in the seven samples of air pollution control residue investigated in this study (% of total dry mass) [1]

Al	Ca	Fe	K	Mg	Na	P	Pb	Si	Ti	Zn	Cl	S
1.4	26	0.69	3.0	0.60	3.0	0.42	0.16	0.54	0.14	0.64	18	1.4

3.2 Separation of Magnetic Material

To enable investigation of the relevance of magnetite to Zn speciation in APCRs, magnetic material was extracted from APCR sample A3 by dipping a plunger magnet into a suspension of ground (<63 μm) APCR in water. Since magnetite is practically insoluble in pH 5 HCl at room temperature[33], the collected material was acid-washed to separate magnetite from other agglomerated soluble phases before drying at 60°C.

3.3 Partial Neutralisation to Target pH 9

To mimic the blending of APCR with waste acid practiced by industry, the pH of a 20 g subsample of each APCR was adjusted with a solution of analytical grade HCl at a liquid-to-solid (L/S) ratio of 1 L/kg. Between 6.0 and 10.5 meq/g of acid (depending on the APCR) were added gradually over a period of 4h, to a target pH of 9. The samples continued to react after the 4h acid addition period and the actual final pHs were higher than 9. For simplicity, the following text refers to the partially neutralised APCR samples by their target "*pH 9*"; the original APCR samples are identified as *raw*.

It is important to note that this was a pH adjustment process intended to approximate industrial practice, not a washing process. There was no separation of a liquid leachate phase,

View Article Online
DOI: 10.1039/D5EM00651A

but the samples were substantially dried by the strong exotherm associated with the neutralisation reaction, leaving all elements and species (apart from water) associated with the solid "pH9" APCRs.

3.4 pH-dependent Leaching

Water leaching of Zn from the raw APCRs and "pH 9" APCRs A3, 4 and 5 was tested according to BS EN 12457-2:2002[34], using MilliQ water at L/S = 10 L/kg without pH adjustment. The contact time was extended to 48 h for comparability with the pH dependent leaching. pH dependent leaching of the raw APCRs was determined using DD CEN/TS 15364:2006[35], with different additions of analytical grade HNO_3, also at L/S = 10 L/kg.

Parameters of interest were analysed in all water leachates, all leachates over the full pH range for raw APCR A3, and the three leachates with pH values closest to pH 4, pH 7 and pH 10 for the other raw APCRs. Leachates were preserved to pH <2 with HNO_3 and analysed by inductively coupled plasma optical emission spectrometry/mass spectrometry (ICP OES/MS); anions in water leachates were determined by ion chromatography. Leached solids from were dried at 60°C for mineralogical characterisation and are further referred to as *leached* APCRs.

The pH, Eh, anion and cation concentrations determined in the leachates were used in chemical equilibrium calculations using the software PHREEQC[36]. Saturation indices were calculated for candidate minerals that might control Zn concentrations in the leachates at six different pH values for raw APCR A3. Thermodynamic data for ZnO, $Zn(OH)_2$, $Zn_2(OH)_3Cl$, $Zn_5(OH)_8Cl$ and $ZnCO_3.H_2O$ were from the WATEQ4F database; data for $ZnFe_2O_4$ were reported by and for $Zn_5(CO_3)_2(OH)_6$ by Preis and Gamsjäger[37]. Saturation indices could not be included for Zn in glass or solid solution (e.g., in apatite or other spinels). The Davies equation was used to calculate activity coefficients in the high ionic strength leachates (i.e., total dissolved solids concentration of 13-40 g/L). Minerals with saturation indices from -1 to +1 were considered to be the potential solubility controlling minerals.

3.5 X-Ray Absorption Spectroscopy

X-ray absorption near edge structure (XANES) and extended x-ray absorption fine structure (EXAFS) spectroscopic analysis for Fe and Zn in all raw APCRs, the magnetic fraction of APCR A3, and Zn in "pH 9" APCRs 1, 8 and 9, and leached APCRs A3 and 9, was performed at Louisiana State University's synchrotron research facility, the J. Bennett Johnston, Sr., Center for Advanced Microstructures and Devices (CAMD), USA [38]. XANES spectra were measured for five different subsamples of APCR A3 to get a better understanding of the micro-scale variability of speciation in the APCR.

CAMD is a second-generation electron storage ring source operating at 1.3 GeV. Zn K-edge measurements were conducted at the High energy X-ray Absorption Spectroscopy (HEXAS) (4.5-25 keV) and Wavelength Shifter Double Crystal Monochromator (WDCM) beamlines (7-18 keV), located on an 11-pole wiggler and a 1-pole wavelength shifter, respectively, that use water-cooled double crystal monochromators [38]. The Hexas monochromator has a pair of Ge 220 crystals, while the WDCM monochromator has a channel-cut Si 111 crystal. The beam dimension was 1 mm (height) x 10 mm (width). The monochromators were calibrated at 7112.0 eV and 9659.0 eV with the K absorption edges of Fe and Zn foils, respectively. Most XAS (combined XANES and EXAFS) scan at CAMD consisted of (with respect to the absorption edge): 5 eV steps from -200 eV to -30 eV, 0.25 eV (0.3 eV for Zn) steps from -30 eV to 30 eV, 1 eV steps from 30 eV to 100 eV, and 0.05 k (wavenumber) steps from 100 eV to 12.0 k (7655 eV for Fe and 10202 eV for Zn). The acquisition time was 3-5 s depending on the concentration for each scan and at least three scans were acquired to obtain good signal to noise ratio. A standard foil was always maintained between the 2nd and 3rd ionization chambers.

View Article Online
DOI: 10.1039/D5EM00651A

Given the indications in the literature of the relevance of spinels to Zn speciation in materials of this kind, the speciation of Fe in the APCRs was assessed by comparing their Fe K-edge XANES and EXAFS spectra with those of spinel reference materials: magnetite, franklinite ($ZnFe_2O_4$) and $NiZnFeO_4$, and also ferrihydrite.

The speciation of Zn in the APCRs was assessed by comparing their Zn K-edge XANES and EXAFS spectra with those of Zn reference materials. Based on previous findings (Table 1), the reference materials selected for the experiments at CAMD were: ZnO (zincite), $Zn(OH)_2$, $Zn_5(CO_3)_2(OH)_6$ (hydrozincite, Avocado Research Chemicals Ltd A14590), $ZnCO_3$ (smithsonite), $ZnCl_2$, $ZnSO_4{\cdot}7H_2O$, $Zn_3(PO_4)_2{\cdot}H_2O$ (hopeite), $ZnAl_2O_4$ (gahnite), $ZnFe_2O_4$ (franklinite), Zn_2SiO_4 (willemite), $Zn_4Si_2O_7(OH)_2{\cdot}H_2O$ (hemimorphite) and a reference glass containing 7870 mg/kg of Zn (Corning Glass IR-X, Smithsonian NMNH 117085) and Zn foil. Zinc chloride hydroxide (confirmed by X-ray diffraction [XRD] as simonkolleite; $Zn_5(OH)_8Cl_2{\cdot}H_2O$) was synthesised in the laboratory by adding 10 g of $ZnCl_2$ to 50 mL of MilliQ water, heating to 80°C, adding 0.59 g of ZnO nanopowder, aging for 24 h at 80°C, washing with acetone and drying at room temperature. Reference materials were measured in transmission and the APCR samples in fluorescence.

Three software packages, Athena in Demeter, Larch, and SixPack were used for principal component analysis (PCA), linear combination fitting (LCF), and target transformation[39-41]. PCA was performed over the range 9640 to 9760 eV. The spectra were decomposed into orthogonal principal components, each associated with an eigenvalue representing the variance explained by that component, where both eigenvalue and variance represent the amount of spectral variation captured by each principal component. Components with higher eigenvalue and variance explain more of the dataset's structure and are therefore more significant. The number of significant components was determined using Malinowski's factor indicator function (IND) [42, 43]. LCF was performed with Athena over the range -20 to 30 eV around the absorption edge. The combinatorial option was used for LCF, including all the phases with reasonable SPOIL values from target transformation, in which SPOIL is a target transformation metric quantifying the mismatch between the reconstructed and experimental spectra [42-44].

To gain insight into Zn coordination environment, curve fitting was used to fit theoretical spectra of Zn standards (i.e., ZnO and $ZnCl_2$) to the experimental Zn spectra of APCR A3 and APCR A8 pH9.57, as representative samples, by adjusting EXAFS variables, including coordination number N, interatomic distance shift ΔR, energy shift ΔE_0, amplitude reduction factor $S0_2$, and mean-square disorder of neighbour distance σ^2 ($Å2{\times}10^{-3}$).

3.6 X-Ray Fluorescence

X-ray fluorescence (XRF) spectra of APCR A3 and its magnetic fraction were obtained at CAMD at the end of an XAS run, at 10211 eV, for 200 seconds, using the same silicon drift detector. Since the spectra were collected in air, the low-Z elements below Ar were not observed. The spectra were normalized to the argon peak (from air, 1.28% by weight)[45]. Since the experimental parameters were identical between measurements, they could be used for semi-quantitative analysis.

4 RESULTS

4.1 Magnetic Fraction of Air Pollution Control Residues

Application of the plunger magnet to the aqueous suspension of APCR A3 followed by acid washing collected about 3% of the total amount of APCR. This magnetic fraction is denoted MF in figures and related discussion. If all the iron in A3 were speciated as magnetite, this would only be ~1% of A3; therefore, MF clearly contains other materials, with quartz, hematite, and amorphous materials prominent in the XRD pattern (Figure A1, Appendix A).

The Fe K-edge XANES spectrum of MF is shown in Figure 1a, for comparison with the spectra of the spinel reference materials. The pre-edge peak intensity (along AA') depends on

the amount of divalent iron in tetrahedral coordination. The intensity is low in franklinite and higher in other spinels, including MF. The relatively high energy of the MF absorption edge indicates that much of the Fe is oxidised (ferric), i.e., that many of the tetrahedral spinel sites are filled by divalent cations other than iron, e.g., Mg, Mn, Cu, Ni, as well as Zn. The white line, along BB', is much sharper in franklinite than in magnetite. The peak intensities beyond the white line (BB') seem to be directly proportional to the atomic number of the cation, being higher for Zn and Ni. For example, the peak along the line CC' is present in the spectra of franklinite and nickel-zinc spinel but absent in that of magnetite. Given the large number of elements, at different concentrations in APCR, that can potentially substitute for Fe in spinels,

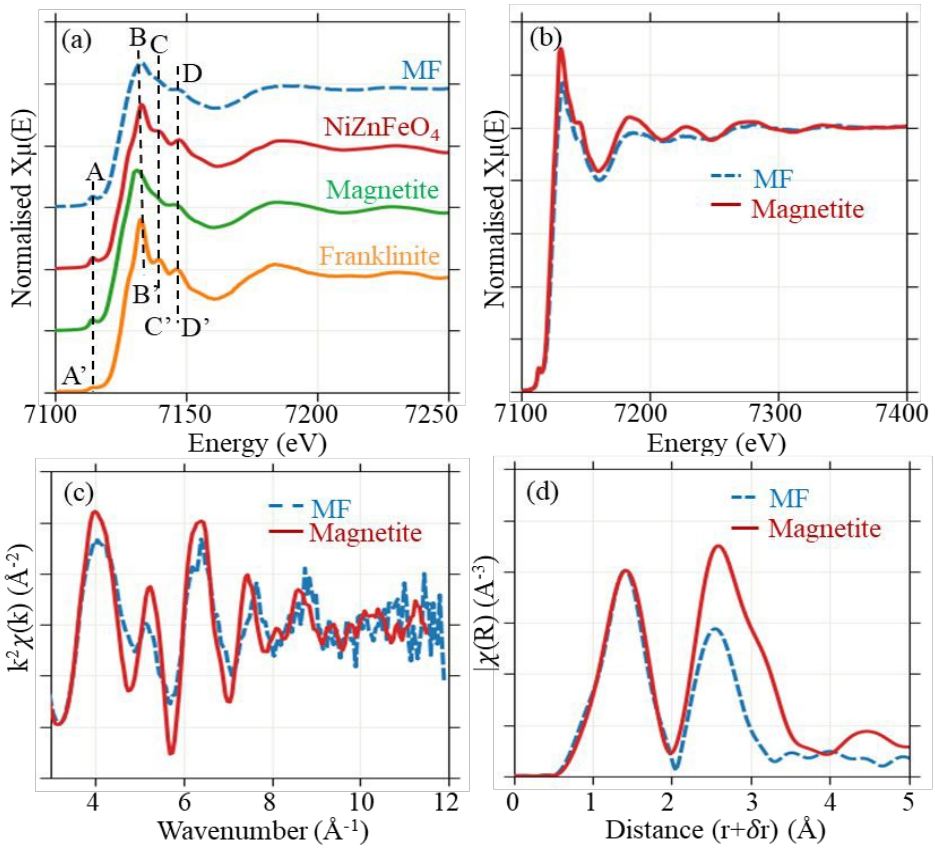

Figure 1 *a*) Fe K-edge XANES spectra of the magnetic fraction of APCR A3 (MF) and some standard spinels; *b)* Fe K-edge EXAFS spectra of MF and the magnetite reference material, also *c*) in k space; and *d*) in Fourier transform of the EXAFS spectra (uncorrected for phase shift), with an interval k = 3-12 Å^{-1} and a Hanning window.

the likelihood of finding a spinel reference material with a spectrum that exactly matches that of MF is low. The Fe K-edge spectrum for MF can be considered to represent an "APCR spinel", which is more similar to magnetite than franklinite or the nickel-zinc spinel. Of course, compositional differences within and among APCRs will yield a range of slightly different spinels.

The Fe K-edge EXAFS spectra of the APCR spinel (MF) and the magnetite reference material are shown in Figure 1b. Though peak locations are very similar, their amplitudes are weaker for MF than for magnetite. This is also seen in k space (Figure 1c). The Fourier transforms of these spectra (Figure 1d) are all similar, having two shells corresponding to the Fe-O and Fe-(Fe, Zn) distances. The peak for the second shell in MF has a lower amplitude compared to the magnetite reference material. This may be due to higher disorder in the crystallites (Debye-Waller factor) or lower coordination, or both, indicating that MF is poorly crystalline.

View Article Online
DOI: 10.1039/D5EM00651A

The XRF spectra of APCR A3 and its magnetic fraction (MF) are shown in Figure 2. Semi-quantitative analysis indicates that Fe is enriched by a factor of 57, and Zn by a factor of 1.7, in MF relative to the raw APCR. Cu, Ti, Ni, Mn and Cr are also enriched in MF (by factors of 4, 6, 36, 17 and 15, respectively).

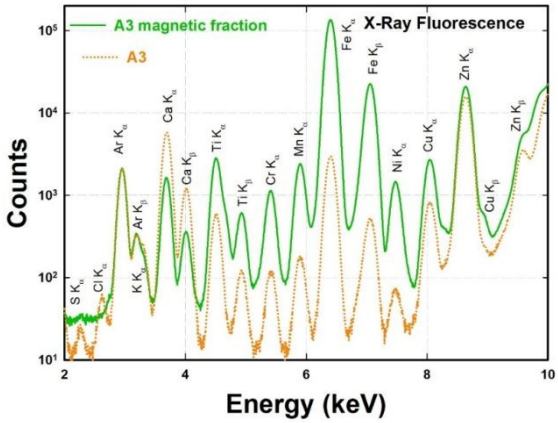

Figure 2. X-ray fluorescence spectra of APCR A3 and its magnetic fraction (MF)

4.2 Iron Speciation in Air Pollution Control Residues

The Fe K-edge XANES and EXAFS spectra of the raw APCRs are shown in Figures 3a, c and d. In Figure 3a, Fe K-edge XANES spectra of the raw APCRs are characterized by a weak pre-edge peak (along AA'), very similar white line shape, intensity and location (along BB'), and a weak bulge at higher energy (CC'). The spectra are very similar; any differences are due to the proportions of different Fe-bearing phases. In Figure 3c, Fe K-edge EXAFS spectra of the raw APCRs are dominated by one single sinusoidal oscillation with similar frequencies and amplitude. This feature corresponding to only one dominant peak centred at approximately 1.35 Å, with comparable intensities in their Fourier Transform spectra (Figure 3d).

Table 3. Proportions of ferrihydrite and magnetite determined by linear combination fitting of raw APCR Fe K-Edge XANES Spectra

APCR	Ferrihydrite	APCR spinel (MF)	R-Factor (x 10^{-3})
1	0.13	0.87	4.0
2	0.69	0.31	1.8
A3	0.52	0.48	1.2
4	1.00	0.00	3.0
5	0.00	1.00	5.2
9	0.62	0.38	2.0
Average	0.49	0.51	

PCA of the XANES spectra indicates that two components justify more than 99% of the variation, and target transformation suggests that ferrihydrite and magnetite are indeed present in these samples (Figure A2, Appendix A). The IND value from PCA corroborates this observation (Figure A2c, Appendix A). A better fit was obtained by using the APCR spinel (MF) spectrum instead of the magnetite reference spectrum. LCF results for the XANES spectra for different APCRs with these two components indicate that Fe may be fully taken up in either ferrihydrite or spinel, or divided between the two (Table 3); it is probable that the

proportions of ferrihydrite and spinel vary within, as well as between, APCRs. Figure 3b illustrates the excellence of the LCF fit.

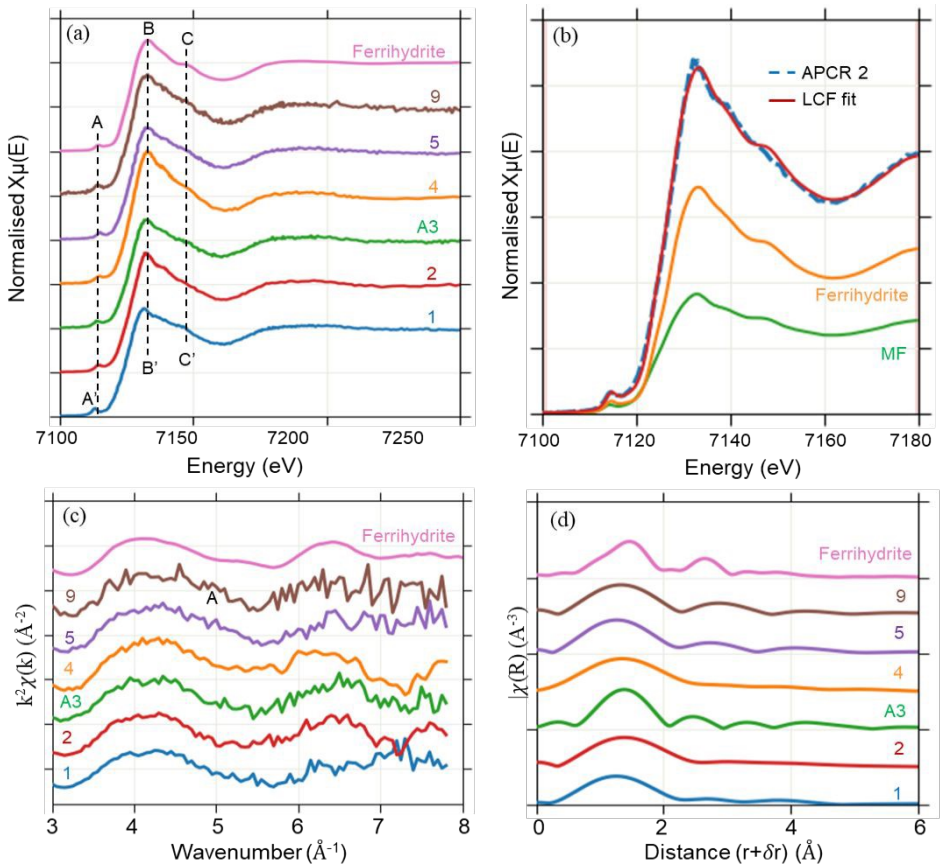

Figure 3. *a*) Fe K-edge XANES spectra of raw APCRs and ferrihydrite; *b*) Linear combination fitting of Fe K-edge XANES spectrum of APCR 2; *c)* Fe K-edge EXAFS spectra of raw APCRs and ferrihydrite; and *d*) Fourier transform of the EXAFS spectra (uncorrected for phase shift), with an interval k = 3-7 Å^{-1} and a Hanning window.

4.3 Zinc Speciation in Air Pollution Control Residues

Figure 4a shows the zinc K-edge XANES spectra of raw APCR A3, MF, and franklinite. Franklinite is the relevant end member for Zn solid solution in spinel, and has a much higher concentration of Zn (26% by mass) than MF (maximum 6% by mass, if Zn were not also present in other species). Zn K-edge XANES spectra of spinels from an industrial hazardous waste incinerator ash melting slag (1.8% Zn) and a Class C coal fly ash (0.013% Zn) are also included for comparison. The Zn spectrum for franklinite has a broad white line consisting of multiple weaker peaks. That of gahnite ($ZnAl_2O_4$) (not shown) is similar, but the weaker peaks are at different energies and of different intensities. The Zn spectra of the spinels from the coal fly ash and the industrial slag have different white line structures, possibly depending on zinc concentration. The Zn spectrum of MF has a broad white line similar to that of franklinite, but the smaller peaks have different intensities at different energies. The Zn EXAFS oscillations their Fourier transforms are shown in Figures 4b and c, respectively. Only one oscillation is dominant for Zn in the raw APCR while multiple oscillations can be seen for Zn in MF and franklinite in k space. This resemblance is also evident in the Fourier transforms where two shells are seen for MF (and the industrial slag coal fly ash), at similar distances as for franklinite.

View Article Online
DOI: 10.1039/D5EM00651A

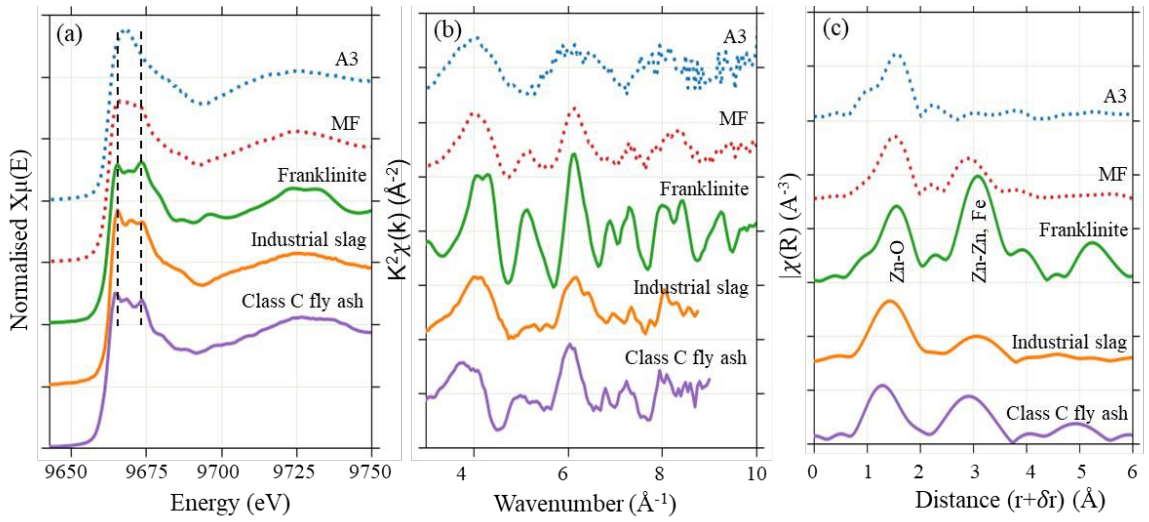

Figure 4. *a)* Zinc K-edge XANES spectra of raw APCR A3 and its magnetic fraction (MF) along with those of franklinite, an industrial slag and Class C fly ash; *b)* EXAFS in k space of the same samples; *c)* their Fourier transforms

Figure 5a shows the Zn K-edge XANES spectra of the raw APCRs. The K-edge absorption energy spreads over a narrow range from 9662.02 eV to 9662.67 eV, and the white line position changes slightly from 9667.62 eV to 9668.62 eV. The white line appears broad in some (APCR 2) while it is slightly sharper in others (APCR A3). The differences among the spectra apparent along the lines AA', BB' and CC' must be due to the proportions of different zinc-bearing phases in the raw APCRs. In Figure 5b, the Zn K-edge APCR EXAFS spectra also appear broadly similar to each other in k space; minor differences can be observed at wavenumbers marked by the lines DD', EE', FF', and GG', which again relate to the contributions made by different phases. In Figure 5c, the Fourier Transform of Zn K-edge APCR EXAFS spectra all present one dominant peak at a distance of around 1.5 Å.

Based on the Zn K-edge XANES spectra of the APCRs and reference materials, PCA was first used to determine that there appear to be three significant phases present in the raw APCRs (Table 4). Target transformation analysis was then used to determine the phases likely to be present (Table 5). The SPOIL value for the spectrum MF, the spinel from APCR A3, is lower than that of the franklinite reference materials, which reveals the similarity among the spinels in the APCRs. $ZnCl_2$ has the lowest SPOIL value, but the Zn K-edge EXAFS spectra (Figure 5b) are dominated by a single strong oscillation, which matches the Zn-O shell in Corning Glass IR-X or $Zn_3(PO_4)_2 \cdot xH_2O$ better than the Zn-Cl shell in $ZnCl_2$, so $ZnCl_2$ can be present in only a very minor amount. This is supprted by the distance of the first peak in the Fourier Transform of APCR A3, which is close to that of hydrozinicte (Zn-O) and much shorter than that of zinc chloride (Zn-Cl) (Figure 5d).

LCF for the Zn K-edge XANES spectra was then performed to estimate the proportions of the potential zinc-containing phases present in the APCRs. The LCF results in Table 6 include the spectra measured for five subsamples of A3 (Figure A3, Appendix A); A3i is the sample referred to elsewhere in this paper. Figures 5b and c show the convincing fits for the two APCRs with the lowest (APCR A8) and highest (APCR 2) R-factors. The sum EXAFS spectra based on the proportions determined by LCF (Table 6) confirm good fit (e.g., for APCRs A8 and 2, in Figure A4, Appendix A). As illustrated in Figure 6 for hydrozincite, linear normal probability plots for each of the identified mineral phases indicate that all of the APCR samples and subsamples belong to the same population (Figure A5, Appendix A). The different

mineral proportions determined by LCF are thus a consequence of microscale APCR heterogeneity rather than real differences between the APCRs.

Curve fitting to theoretical standard was performed to fit theoretical spectra (i.e., ZnO with tetrahedral Zn-O and $ZnCl_2$ with tetrahedral Zn-Cl), respectively, to the experimental one of raw APCR A3, shown in Figure A6 & Figure A7, Appendix A. The same fitting was conducted to the experimental spectra of ZnO and $ZnCl_2$, shown in Figure A8 & Figure A9, Appendix A. The best fit results (Table A1 and Figure A6 a & b, Appendix A) show that the first shell of APCR A3 was obtained with a coordination number of 4.1 at a distance of 1.943 Å ($S_0^2 = 0.93$ [46]; $E_0 = 0.21$ eV; $\Delta R = -0.034$ Å; Debye-Waller factor = 0.005; R-factor = 0.009). The fit results of APCR A3 with $ZnCl_2$ have a significantly higher R-factor of 0.042, approximately three times larger than obtained with ZnO, indicating a poor fit result. Zn in APCR A3 is, therefore, predominantly tetrahedrally coordinated with oxygen atoms, rather than with chloride atoms.

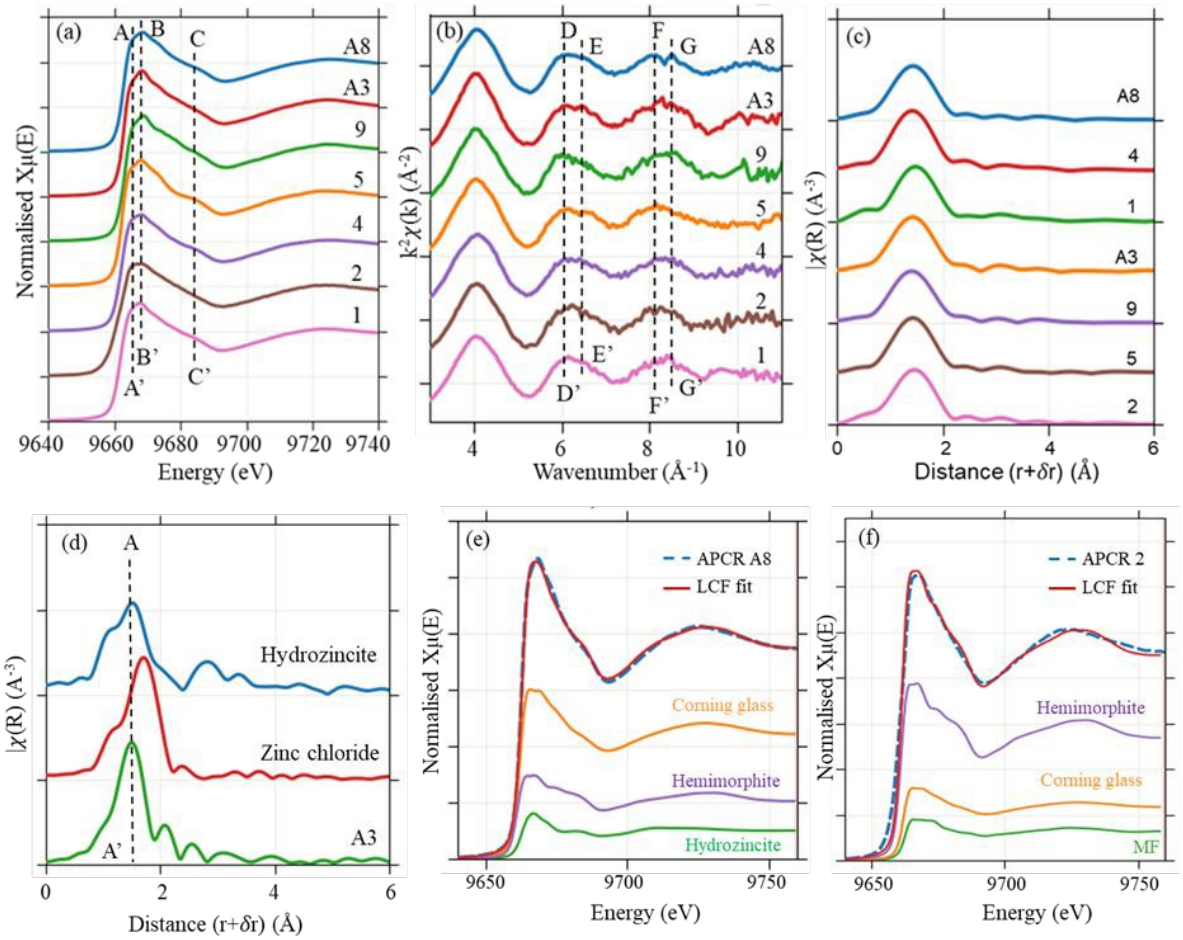

Figure 5. *a*) Zn K-edge XANES spectra of raw APCRs; *b*) Zn K-edge EXAFS spectra of raw APCRs; *c)* Fourier Transform of the EXAFS spectra; *d)* and *e)* linear combination fitting of APCR 9 and 2, respectively

View Article Online
DOI: 10.1039/D5EM00651A

Table 4. Principal component analysis of Zn K-Edge XANES of raw APCRs

Component	Eigenvalue	Variance	Cumulative Variance	IND
1	82.90	0.938	0.938	0.04025
2	3.31	0.037	0.975	0.02301
3	1.17	0.013	0.988	0.01662
4	0.40	0.004	0.993	0.02229
5	0.25	0.002	0.996	0.04242
6	0.20	0.002	0.998	0.12690
7	0.13	0.001	1.0	NA

Table 5. Target transformation of potential phases from Zn K-Edge XANES

Phase	Chi Square	R Value	SPOIL
$ZnCl_2$	0.69760	0.00068	0.9185
Corning Glass IR-X	0.14646	0.00014	1.3122
hemimorphite	0.50872	0.00054	1.6640
hydrozincite	1.74022	0.00164	2.1260
hopeite	1.13807	0.00117	2.5550
willemite	0.86481	0.00093	3.7450
MF	0.45643	0.00045	3.9522
franklinite	1.97155	0.00165	4.0789

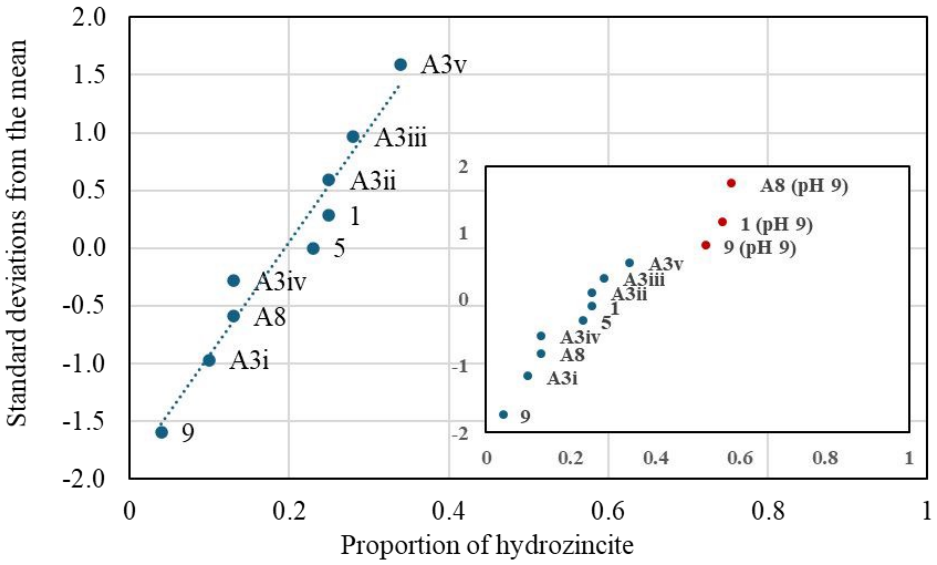

Figure 6. The linear cumulative normal probability plot of hydrozincite proportions in all raw APCR samples containing hydrozincite (main) indicates that they belong to the same population. The inset shows significantly increased proportions of hydrozincite in APCRs neutralised to a target pH of 9

View Article Online
DOI: 10.1039/D5EM00651A

Table 6. Mineral proportions determined by linear combination fitting of Zn K-edge XANES spectra of APCRs

APCR	Hemim (Zn_4Si_2	Cornin	Hopeit ($Zn_3(P$	Hydroz ($Zn_5(C$	R-factor x 10^3
a) Raw APCRs					
1	0.72		0.03	0.25	0.3
2	0.14	0.61	0.25		3
4	0.32		0.32	0.35	0.4
5	0.61		0.16	0.23	2.9
A8		0.29	0.6	0.13	0.14
9	0.32	0.64		0.04	0.12
Average*	0.35	0.57	0.33	0.19	0.16
Standard Deviation*	0.19	0.19	0.19	0.23	0.10
b) Subsamples of APCR A3					
A3i	0.35			0.55	0.1
A3ii	0.39	0.36			0.25
A3iii	0.48		0.24		0.28
A3iv			0.87		0.13
A3v	0.49		0.17		0.34
Average	0.38	0.37	0.36	0.32	0.19
Standard Deviation	0.11	0.19	0.29	0.20	0.10
c) pH 9 APCRs					
1	0.15		0.3	0.56	8
A8	0.09	0.33		0.58	4
9	0.16	0.32		0.52	1.4
Average	0.16	0.19	0.33	0.30	0.55
Standard Deviation	NA	0.12	NA	NA	0.03
Overall Average	0.37	0.36	0.37	0.31	0.31
Overall Std Dev	0.16	0.23	0.25	0.21	0.17

4.4 Zinc Speciation in the "pH 9" and leached Air Pollution Control Residues

The Zn K-edge XANES spectra of raw APCRs A8, 9 and 1 can be compared with those of the same APCRs neutralised to a target pH of 9 in Figure 7a (without separation of a leachate). The increased prominence of the features labelled A, B and C in the "pH 9" APCRs indicates changes in speciation. Differences in the white line regions of the "pH 9" APCRs also reveal differences in phase composition. The Zn K-edge spectra of the "pH 9" samples do not show any resemblance to zinc chloride or oxy-chloride, despite a large amount of chloride in the system from the APCR itself and the addition of HCl. Normal probability plots of the mineral proportions determined by LCF in the "pH 9" APCRs along with the raw APCRs show a significantly increased proportion of hydrozincite (Figure 6, inset). The proportions of hemimorphite (particularly), spinel and glass, are lower in the "pH 9" than raw samples,

View Article Online
DOI: 10.1039/D5EM00651A

although the difference is not statistically evidenced (Figure A5, Appendix A), suggest that these poorly crystalline species have been altered to hydrozincite.

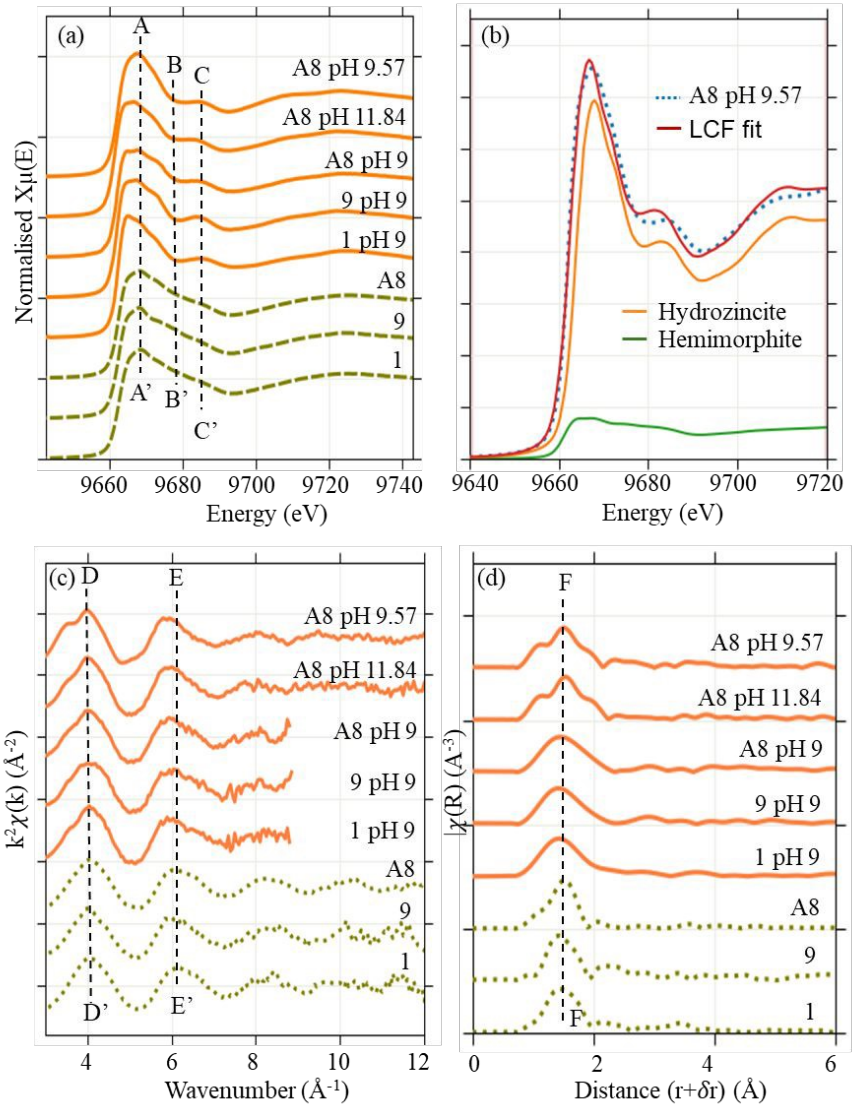

Figure 7. a) Zn K-edge X-ray XANES spectra for raw APCRs 1, 9 and A8, compared with the "pH 9" APCRs after partial neutralisation with HCl (without leachate separation), as well as APCR 8 after leaching with water at unadjusted pH 11.84, and diluted HNO_3 at pH 9.57 (after leachate separation); b) comparison of the latter spectrum with hydrozincite, and the linear combination fit based on hydrozincite and hemimorphite. ; *c)* Zn K-edge EXAFS spectra for raw APCRs; and *d*) in Fourier transform of the EXAFS spectra (uncorrected for phase shift), with an interval k = 3-8.7 $Å^{-1}$ for A8 pH9, 9 pH9 and 1 pH9, and k = 3-12 $Å^{-1}$ for the remaining raw APCRs and a Hanning window

Zn K-edge XANES spectra of APCR A8 after leaching with water at an unadjusted pH of 11.84, and after leaching with diluted HNO_3 at pH 9.57 (both after leachate separation) are also show in Figure 7a. These spectra can be observed to be very similar to those of the "pH 9" APCRs. Zn K-edge EXAFS spectra of the same samples and their Fourier Transform spectra are present in Figures 7c and d, and the observation is consistent with the XANES result. A comparison of the Zn K-edge XANES spectrum of leached APCR A8 at pH 9.57 with that of

hydrozincite (Figure 7b) shows a very strong resemblance, and the LCF results indicate that the sample is 88% hydrozincite and 12% hemimorphite. The best LCF fit of Zn K-edge XANES spectrum for APCR A8 (pH 9.57) in the presence of zinc chloride, yielded a poor fit (Figure A10, Appendix A), indicating that only a very minor amount of zinc chloride is present in the sample.

Curve fitting to theoretical standards was performed to fit theoretical spectra (i.e., ZnO with tetrahedral Zn-O and $ZnCl_2$ with tetrahedral Zn-Cl), respectively, to the experimental one of raw APCR A8 pH 9.57, shown in Figure A11 & Figure A12, Appendix A. The best fit results (Table A1 and Figure A11 a & b, Appendix A) show that the first shell of APCR A8 pH 9.57 was obtained with a coordination number of 5.1 at a distance of 2.012 Å (S_0^2 = 0.93 [46]; E_0 = 2.36 eV; ΔR = 0.048 Å; Debye-Waller factor = 0.012; R-factor = 0.014). The fit results of APCR A8 pH 9.57 with $ZnCl_2$ have a significantly higher R-factor of 0.120, approximately nine times larger than obtained with ZnO, indicating a poor fit result. Zn in APCR A8 pH 9.57 is, therefore, predominantly coordinated with oxygen atoms, rather than with chloride atoms.

4.5 Zinc Leaching from Raw and "pH 9" APCRs

Zn leachability from the raw APCRs in BS EN 12457-2:2002 [34] and DD CEN/TS 15364:200 [35], and "pH 9" APCRs A3, 4 and 5 in BS EN 12457-2:2002, has been plotted as a function of pH in Figure 8; 1 mg/kg leached from the solid equates to 1.5 mM. The pHs of the water-based leachates ranged from 11.83-12.36 for the raw APCRs, and the actual pHs of the "pH 9" APCRs ranged from 10.0-10.7 as the samples continued to react following initial adjustment to the target pH of 9 with HCl. The "pH 9" APCRs dis-agglomerated when immersed for leaching, and the leachate concentrations for the raw APCRs and "pH 9" APCRs fall along the same curve in Figure 8.

Table 7 presents saturation indices calculated using PHREEQC for candidate solid phases that may have controlled the observed leachate concentrations in the pH-dependent leaching of raw APCR A3. The main contributors to the charge balance were Ca^{2+}, Na^+, K^+, Cl^- and SO_4^{2-}. A small shortage of anions (2-5%) is likely to be carbonate ion in this pH range. The phases with saturation indices closest to 0 at alkaline pH were $Zn(OH)_2$, or possibly ZnO, and it therefore seems likely that these phases controlled the concentrations of Zn in the leachate by precipitation. These results are consistent with the findings of previous workers in Table 1. Interestingly, at pH 9.57, the present work also shows possible control of the leachate concentration by $Zn_5(OH)_8Cl$, which was also determined by Zhang et al. (2006) at pH ~8, or $Zn_5(CO_3)_2(OH)_6$, which is consistent with our XAS findings regarding Zn speciation in the solid.

View Article Online
DOI: 10.1039/D5EM00651A

Table 7. Saturation indices for the pH-dependent leaching of APCR A3 according to DD CEN/TS 15364:2006

	Leachate pH					
Species	2.98	5.72	8.77	9.57	11.55	11.84*
Zincite (ZnO)	-	-2.7	-0.72	0.72	0.98	1.1
$Zn(OH)_2$	-	-3.3	-1.3	0.1	0.37	0.47
$Zn_2(OH)_3Cl$	-	-4.6	-3.7	-1.7	-3.1	-3.7
Simonkolleite ($Zn_5(OH)_8Cl$)	-	-	-	0.44	-2.2	-2.2
$ZnCO_3 \cdot H_2O$	-	-	-3.2	-3.3	-	-
Smithsonite ($ZnCO_3$)	-	-	-3.4	-3.6	-	-
Hydrozincite ($Zn_5(CO_3)_2(OH)_6$)	-	-	-4.6	-0.6	-4.8	-4.7
Willemite (Zn_2SiO_4)	-	-3.9	2.5	-	-	-
$ZnSiO_3$	-1.5	-2.0	2.5	4.7	4.1	4.1
Franklinite ($ZnFe_2O_4$)	-	-	-	-	-	-
Solid phases likely to control solution concentrations (-1 < saturation index < 1)						

* water leachate

"-" indicates phases highly unlikely to control solution concentrations with 5 < saturation index < - 5

394

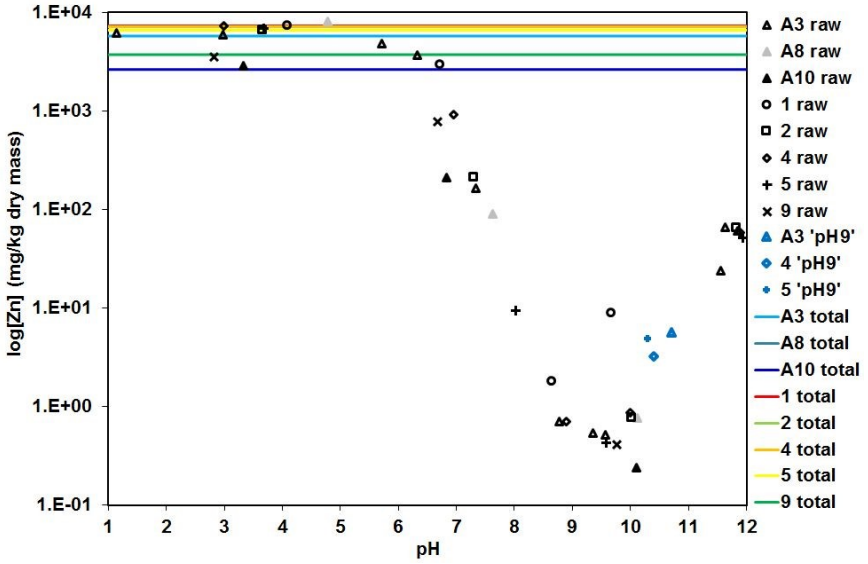

Figure 8. Zn leachability from seven APCRs as a function of pH compared with total Zn concentrations (BS EN 12457-2:2002 and DD CEN/TS 15364:2006 results for raw APCRs, and BS EN 12457-2:2002 results for pH 9 APCRs)

View Article Online
DOI: 10.1039/D5EM00651A

5 Discussion

5.1 Raw Air Pollution Control Residues

The results of PCA and LCF of Zn K edge XANES (Table 6) show several phases present in the raw APCRs in significant and varying proportions: i) a spinel phase, ii) a glassy or crystalline silicate phase; iii) a phosphate phase, and iv) hydrozincite. All Zn-K edge APCR EXAFS spectra are dominated by a single strong oscillation, which is consistent with poor crystallinity of the identified phases, and presence of Zn in solid solution and glass. This oscillation matches the Zn-O shell better than the Zn-Cl shell, indicating that Zn chlorides can be present in only a very minor amounts. This finding contrasts with those of other researchers (Table 1).

Fe K-edge XANES showed that Fe in the raw APCRs is distributed between magnetite and ferrihydrite, in variable proportions from 0 to 100%. Enrichment of Zn, Cu, Ti, Ni, Mn and Cr in the magnetic fraction compared to the raw APCR is consistent with findings by De Boom, *et al.*[47] for MSW incinerator ashes, and Wang[48] and Kukier, *et al.*[49] for the magnetic fraction of coal fly ash. While Zn K-edge XANES and EXAFS of the magnetic fraction of UK APCR show a structure most similar to that of magnetite, there is also a resemblance to franklinite (which was identified in APCRs by others[6, 14, 21]). Yu, *et al.*[17] did not include $ZnFe_2O_4$ in their fit, but speculated that fit would be improved by its inclusion. Zn K-edge XANES for Swedish MSW incinerator ashes and APCRs clearly indicates the presence of franklinite [6, 21]. Our study of the magnetic fraction of APCR clearly shows the presence of a zinc-substituted magnetite, for which an identical reference material would be difficult to obtain. The absence of more than one main oscillation in the Zn K edge EXAFS spectrum of APCR (Figure 4) also suggests that Zn is not sorbed to ferrihydrate[50], though sorbed Zn has been identified by others[6].

Both hemimorphite ($Zn_4Si_2O_7(OH)_2 \cdot H_2O$) and willemite ($Zn_2SiO_4$), are common in nature, where they may be found with hydrozincite[51] and also in mining and metallurgical wastes[32, 52]. Hemimorphite can be formed from a variety of precursors at relatively low temperature[53]; it dehydrates to willemite at 364-912˚C [54], which decomposes to ZnO and SiO_2 at temperatures unlikely to be encountered in EfW facilities (~1500˚C[55]). Hemimorphite in the APCRs could therefore only form in the fabric filter. Predominance information for hemimorphite over $ZnCl_2$ in the conditions that prevail in APCRs is not available, but willemite predominates over $ZnCl_2$ under alkaline conditions in aqueous systems at ambient temperature and open to the atmosphere[56]. Astrup, *et al.*[8] suggested that willemite also contributed to control of Zn leachability for some APCRs, but this is unlikely in our APCRs, since it was not identified as a main Zn-containing phase in the raw APCR and would not form during the leaching process. Given supersaturation of our leachates with compounds with larger solubility product constants, control of Zn leachability by willemite ($K_{sp} = 10^{-15.33}$ [36]) is unlikely. Si was below the detection limit in our leachates, so neither hemimorphite nor willemite could be included in our modelling. Hemimorphite may control Zn leaching at mildly acidic pH, though it is likely to convert to hydrozincite at low alkaline pH [57].

Apatite ($Ca_6(PO4)_4$) is the most common phosphate mineral on Earth. It forms a wide-ranging solid solution, with Ca being easily replaced by Na, K and other elements including Zn. Zinc phosphate was found by Pattanaik and Huggins[58] in oil fly ash. Several researchers have found that the addition of a phosphate source to different kinds of waste increased retention of zinc, with identification of both ($Zn_3(PO_4)_2$[59] and apatite[60-62]. The amount of P in these UK APCRs ranges from 0.20 to 0.59%. The presence of a phosphate phase containing zinc is thus likely. While the Zn K-edge spectrum for hopeite $Zn_3(PO_4)_2 \cdot H_2O$ contributed to good LCF fits for the Zn K-edge spectra of many of the raw APCRS, there is a similarity between the XANES and EXAFS spectra of apatite[63], so the presence of apatite is also a possibility. Given the many possible compositions of apatite, a reference material with an exactly matching spectrum to any or all of the APCRs would be hard to find.

View Article Online
DOI: 10.1039/D5EM00651A

At the CO_2 partial pressures in EfW flue gas (~0.1), hydrozincite ($Zn_5(CO_3)_2(OH)_6$) is stable only between about 100°C and 150˚C[54]. This suggests that the hydrozincite in APCRs is formed during cooling, i.e., in the fabric filter. Recent research by Rissler et al. also found hydrozincite, and its absence in the findings of previous workers may relate to other operating conditions, e.g., use of electrostatic precipitators that operate at a higher temperature in older plants. Modern operating conditions emphasise a rapid transition from very high operating temperatures (>850˚C) to ambient temperature, to avoid dioxin formation. This temperature regime may also avoid formation of ZnO and $ZnCl_2$. Hydrozincite predominates over $ZnCO_3$ or $Zn(OH)_2$ at pH greater than 7.2 in aqueous systems at ambient temperature and open to the atmosphere[64], i.e., the environment of the raw, "pH 9" and leached APCRs.

5.2 "pH 9" APCRs

Zn K-edge XANES showed convincing evidence of formation of hydrozincite in the "pH9" APCRs treated by partial neutralisation with HCl. Decreased proportions of hemimorphite, spinel and glass in the "pH 9" APCRs compared to the raw samples suggest that the poorly crystalline forms of all of these species have been altered to hydrozincite. However, observation of increased hydrozincite also in the leached APCRs at pH 11.82 and 9.57 suggests that the presence of water to enable dissolution of soluble phases from the raw APCRs is more important for formation of secondary hydrozincite than the partial neutralisation reaction.

Agglomeration of APCRs as a result of partial neutralisation with concentrated acid is sometimes reported in industrial practice at full-scale. It seems to be caused by formation of secondary phases. Since typical industrial methods and contact times are as unlikely to achieve a stable pH of 9 in acid blending as the "pH 9" APCRs produced in our laboratory, which had final pHs from 10.0-10.7, it is possible that the agglomerating phases could include small amounts of thaumasite or calcium silicate hydrate. Substitution of Zn for Ca in the related mineral ettringite ($Ca_6Al_2(SO_4)_3(OH)_{12}\cdot 26H_2O$) has been postulated[65], but the evidence is weak.

Regardless of these potential agglomeration reactions, the fact that Zn leaching data from the raw APCRs and "pH 9" APCRs fall along the same curve in Figure 8 clearly demonstrates that the treatment with concentrated acid does not change the mechanisms that control Zn leachability. Although Zn leachability is decreased by partial neutralisation to pH 10-10.7 (and would be further decreased if a stable pH of 9 could be achieved), this pH is unlikely to prevail in contact with landfill leachate with a typical pH of 5-8. In general, partial neutralisation cannot be considered as a long-term strategy to avoid environmental risk, as a mildly alkaline pH will be neutralised by carbonation and acidification, through interaction with the atmosphere and groundwater.

In the context of assessment of the environmental risks associated with APCRs, our findings should be considered in the context of the toxicity, leachability and bioavailability of the identified Zn phases, whereby our results suggested control of Zn leaching by precipitation of zinc hydroxide, and possibly by dissolution of hydrozincite at intermediate alkaline pH. Molina*, et al.*[66] have found the following sequence of bioavailability: hydrozincite > hemimorphite > zincite ≈ smithsonite >> sphalerite.

6 Conclusions

Zn K-edge XAS studies of magnetic and non-magnetic fractions, supplemented by Fe K-edge XAS, provided a better insight into the speciation of zinc in APCRs, showing that magnetite can be an important repository of zinc and that hemimorphite, glass and zinc phosphate are important Zn-containing phases, along with hydrozincite. The magnetite phase can also incorporate other potential pollutants, including Cu, Ni and Cr. Leaching studies show that with or without treatment by partial neutralisation, the mineral controls on zinc leaching behaviour are the same.

View Article Online
DOI: 10.1039/D5EM00651A

CRediT author contribution statement: Amitava Roy: Methodology, Formal analysis, Investigation, Resources, Data curation, Writing, Visualization, Funding acquisition. Dan Ting Chen: Methodology, Formal analysis, Investigation, Writing, Visualization. Anna Bogush: Methodology, Formal Analysis, Investigation. Julia A. Stegemann: Conceptualisation, Methodology, Formal Analysis, Resources, Writing, Visualisation, Supervision, Project administration, Funding acquisition.

Conflicts of interest

This work was funded by the Environment Agency, UCL CEGE, CAMD, the UK EPSRC (Grant EP/M00337X/1) and the Louisiana Board of Regents (LEQSF(2016-17)-ENH-TR-07). All the authors declare no conflict of interest, either financial or otherwise.

Data availability

The data supporting this article have been included as part of the Supplementary Information.

Acknowledgements

We would like to thank: Paul Fernee and Peter Chesney (Environment Agency) for samples; Kym Jarvis (NERC ICP facility); Judith Zhou and Ian Sturtevant (UCL CEGE laboratory); and the Smithsonian National Museum of Natural History, for the glass standard.

Abbreviations

EfW, energy from waste; MSW, municipal solid waste; APCR, air pollution control residue; XRD, X-ray powder diffraction; XANES, X-ray absorption near edge structure; EXAFS, extended X-ray absorption fine structure; CAMD, J. Bennett Johnston, Sr., Center for Advanced Microstructures and Devices; ICP OES/MS, inductively coupled plasma optical emission spectrometry/mass spectrometry; PCA, Principal component analysis; UCL, University College London; XAS, X-ray absorption spectroscopy;

References

1. A. Bogush, J. A. Stegemann, I. Wood and A. Roy, Element composition and mineralogical characterisation of air pollution control residue from UK energy-from-waste facilities, *Waste Management*, 2015, **36**, 119.
2. L. S. Morf, P. H. Brunner and S. Spaun, Effect of operating conditions and input variations on the partitioning of metals in a municipal solid waste incinerator, *Waste Management and Research*, 2000, **18**, 4–15.
3. A. Jakob, S. Stucki and P. Kuhn, Evaporation of heavy metals during the heat treatment of municipal solid waste incinerator fly ash, *Environmental Science & Technology*, 1995, **29**, 2429–2436.
4. W. Seeker, W. Lanier and M. Heap, Municipal waste combustion study: Combustion control of organic emissions, *EPA, Research Triangle Park, NC*, 1987.
5. B. J. Stuart and D. S. Kosson, Characterization of municipal waste combustion air pollution control residues as a function of particle size, *Combustion science and Technology*, 1994, **101**, 527–548.
6. J. Rissler, K. K. Fedje, K. Klementiev, B. Ebin, C. Nilsson, H. M. Rui, T. M. Klufthaugen, S. Sala and I. Johansson, Zinc speciation in fly ash from MSWI using XAS-novel insights and implications, *Journal of Hazardous Materials*, 2024, **477**, 135203.
7. T. T. Eighmy, J. D. Eusden, J. E. Krzanowski, D. S. Domingo, D. Staempfli, J. R. Martin and P. M. Erickson, Comprehensive approach toward understanding element

speciation and leaching behavior in municipal solid waste incineration electrostatic precipitator ash, *Environmental science & technology*, 1995, **29**, 629–646.

8. T. Astrup, J. J. Dijkstra, R. N. Comans, H. A. Van der Sloot and T. H. Christensen, Geochemical modeling of leaching from MSWI air-pollution-control residues, *Environmental science & technology*, 2006, **40**, 3551–3557.
9. L. Wang, Q. Chen, I. A. Jamro, R. Li, Y. Li, S. Li and J. Luan, Geochemical modeling and assessment of leaching from carbonated municipal solid waste incinerator (MSWI) fly ash, *Environmental Science and Pollution Research*, 2016, **23**, 12107–12119.
10. H. Zhang, P.-j. He, L.-m. Shao, J.-h. Feng and Q.-k. Cao, Leaching behavior of Pb and Zn in air pollution control residues and their modeling prediction, *Journal of Environmental Sciences (China)*, 2006, **18**, 583–586.
11. L. Le Forestier and G. Libourel, Characterization of flue gas residues from municipal solid waste combustors, *Environmental Science & Technology*, 1998, **32**, 2250–2256.
12. P. Fermo, F. Cariati, A. Pozzi, M. Tettamanti, E. Collina and D. Pitea, Analytical characterization of municipal solid waste incinerator fly ash: Part II, *Fresenius' journal of analytical chemistry*, 2000, **366**, 267–272.
13. R. P. Struis, C. Ludwig, H. Lutz and A. M. Scheidegger, Speciation of zinc in municipal solid waste incineration fly ash after heat treatment: an X-ray absorption spectroscopy study, *Environmental science & technology*, 2004, **38**, 3760–3767.
14. M. Takaoka, T. Yamamoto, T. Tanaka, N. Takeda, K. Oshita and T. Uruga, Direct speciation of lead, zinc and antimony in fly ash from waste treatment facilities by XAFS spectroscopy, *Physica Scripta*, 2005, **2005**, 943.
15. J. Hyks, T. Astrup and T. H. Christensen, Influence of test conditions on solubility controlled leaching predictions from air-pollution-control residues, *Waste Management & Research*, 2007, **25**, 457–466.
16. M. J. Quina, J. C. Bordado and R. M. Quinta-Ferreira, Treatment and use of air pollution control residues from MSW incineration: An overview, *Waste Management*, 2008, **28**, 2097–2121.
17. M. Yu, S. Tian, W. Chu, D. Chen, Q. Wang and Z. Wu, Speciation of zinc in secondary fly ashes of municipal solid waste at high temperatures, *Synchrotron Radiation*, 2009, **16**, 528–532.
18. A. P. Bayuseno and W. W. Schmahl, Characterization of MSWI fly ash through mineralogy and water extraction, *Resources, Conservation and Recycling*, 2011, **55**, 524–534.
19. Y.-M. Zhu, H. Zhang, S.-S. Fan, S.-J. Wang, Y. Xia, L.-M. Shao and P.-J. He, In-situ determination of metallic variation and multi-association in single particles by combining synchrotron microprobe, sequential chemical extraction and multivariate statistical analysis, *Journal of Hazardous Materials*, 2014, **276**, 241–252.
20. X. Bolaños Chamorro, B. Ayati and D. Newport, Chemical characterisation and leaching properties of air pollution control residues (APCr) from municipal solid waste incineration (MSWI) sites in the UK, 2023.
21. J. Rissler, K. Klementiev, J. Dahl, B.-M. Steenari and M. Edo, Identification and quantification of chemical forms of Cu and Zn in MSWI ashes using XANES, *Energy & Fuels*, 2020, **34**, 14505–14514.
22. C. Biagioni and M. Pasero, The systematics of the spinel-type minerals: An overview, *American Mineralogist*, 2014, **99**, 1254–1264.

23. A. V. Carvalho and C. B. Sclar, Experimental determination of the $ZnFe_2O_4$-$ZnAl_2O_4$ miscibility gap with application to franklinite-gahnite exsolution intergrowths from the Sterling Hill zinc deposit, New Jersey, *Economic Geology*, 1988, **83**, 1447–1452.
24. C. Frondel and C. Klein Jr, Exsolution in franklinite, *American Mineralogist: Journal of Earth and Planetary Materials*, 1965, **50**, 1670–1680.
25. Y. Wei, T. Shimaoka, A. Saffarzadeh and F. Takahashi, Mineralogical characterization of municipal solid waste incineration bottom ash with an emphasis on heavy metal-bearing phases, *Journal of Hazardous Materials*, 2011, **187**, 534–543.
26. R. Helmuth, *Fly ash in cement and concrete*, 1987.
27. R. T. Hemmings and E. E. Berry, Speciation in size and density fractionated fly ash, *MRS Online Proceedings Library (OPL)*, 1985, **65**, 91.
28. S. Gomes, M. François, M. Abdelmoula, P. Refait, C. Pellissier and O. Evrard, Characterization of magnetite in silico-aluminous fly ash by SEM, TEM, XRD, magnetic susceptibility, and Mössbauer spectroscopy, *Cement and Concrete Research*, 1999, **29**, 1705–1711.
29. J. A. Stegemann, A. Roy, R. J. Caldwell, P. J. Schilling and R. Tittsworth, Understanding environmental leachability of electric arc furnace dust, *Journal of Environmental Engineering*, 2000, **126**, 112–120.
30. T. Suetens, M. Guo, K. Van Acker and B. Blanpain, Formation of the $ZnFe_2O_4$ phase in an electric arc furnace off-gas treatment system, *Journal of hazardous materials*, 2015, **287**, 180–187.
31. N. M. Piatak, M. B. Parsons and R. R. Seal II, Characteristics and environmental aspects of slag: A review, *Applied Geochemistry*, 2015, **57**, 236–266.
32. A. Manceau, B. Lanson, M. L. Schlegel, J. C. Harge, M. Musso, L. Eybert-Berard, J.-L. Hazemann, D. Chateigner and G. M. Lamble, Quantitative Zn speciation in smelter-contaminated soils by EXAFS spectroscopy, *American Journal of Science*, 2000, **300**, 289–343.
33. P. G. Jeffery, D. Hutchison and P. JEFFREY, *Chemical methods of rock analysis*, Elsevier, 1981.
34. BS EN 12457-2:2002; British Standards Institution, 2002
35. BS DD CEN/TS 15364:2006;, 2006
36. D. L. Parkhurst and C. Appelo, Description of input and examples for PHREEQC version 3—a computer program for speciation, batch-reaction, one-dimensional transport, and inverse geochemical calculations, *US geological survey techniques and methods*, 2013, **6**, 497.
37. W. Preis and H. Gamsjäger, (Solid+ solute) phase equilibria in aqueous solution. XIII. Thermodynamic properties of hydrozincite and predominance diagrams for (Zn2++ H2O+ CO2), *The Journal of Chemical Thermodynamics*, 2001, **33**, 803–819.
38. B. C. Craft, A. M. Findley, G. L. Findley, S. P. McGlynn, J. D. Scott and F. H. Watson, LSU Center for Advanced Microstructures and Devices, *Rev. Sci. Instrum.; (United States)*, 1989, **60:7**.
39. M. Newville, Larch: an analysis package for XAFS and related spectroscopies, presented in part at the Journal of Physics: Conference Series, 2013.
40. B. Ravel and M. Newville, ATHENA, ARTEMIS, HEPHAESTUS: data analysis for X-ray absorption spectroscopy using IFEFFIT, *Synchrotron Radiation*, 2005, **12**, 537–541.
41. S. M. Webb, SIXpack: a graphical user interface for XAS analysis using IFEFFIT, *Physica scripta*, 2005, **2005**, 1011.
42. S. Calvin, *XAFS for Everyone*, CRC press, 2024.

43. E. R. Malinowski and D. G. Howery, *Factor analysis in chemistry*, Wiley New York, 2002.
44. E. R. Malinowski, Theory of error for target factor analysis with applications to mass spectrometry and nuclear magnetic resonance spectrometry, *Analytica Chimica Acta*, 1978, **103**, 339–354.
45. M. Alfeld, V. Gonzalez and A. van Loon, Data intrinsic correction for working distance variations in MA-XRF of historical paintings based on the Ar signal, *X-Ray Spectrometry*, 2021, **50**, 351–357.
46. D. T. Chen, UCL (University College London), 2024.
47. A. De Boom, M. Degrez, P. Hubaux and C. Lucion, MSWI boiler fly ashes: Magnetic separation for material recovery, *Waste Management*, 2011, **31**, 1505–1513.
48. X. S. Wang, Mineralogical and chemical composition of magnetic fly ash fraction, *Environmental Earth Sciences*, 2014, **71**, 1673–1681.
49. U. Kukier, C. F. Ishak, M. E. Sumner and W. P. Miller, Composition and element solubility of magnetic and non-magnetic fly ash fractions, *Environmental Pollution*, 2003, **123**, 255–266.
50. M. Nachtegaal and D. L. Sparks, Effect of iron oxide coatings on zinc sorption mechanisms at the clay-mineral/water interface, *Journal of Colloid and Interface Science*, 2004, **276**, 13–23.
51. V. Coppola, M. Boni, H. A. Gilg, G. Balassone and L. Dejonghe, The “calamine” nonsulfide Zn–Pb deposits of Belgium: petrographical, mineralogical and geochemical characterization, *Ore Geology Reviews*, 2008, **33**, 187–210.
52. P. Iavazzo, P. Adamo, M. Boni, S. Hillier and M. Zampella, Mineralogy and chemical forms of lead and zinc in abandoned mine wastes and soils: an example from Morocco, *Journal of geochemical exploration*, 2012, **113**, 56–67.
53. J. Yang, Y. Sun, Z. Chen and X. Zhao, Hydrothermal synthesis and optical properties of zinc silicate hierarchical superstructures, *Materials Letters*, 2011, **65**, 3030–3033.
54. Z. Ding, Z. Yin, H. Hu and Q. Chen, Comparison of thermal property and dissolution behavior of synthetic compound and natural hemimorphite, *Thermochimica acta*, 2010, **511**, 168–173.
55. M. Takesue, H. Hayashi and R. L. Smith Jr, Thermal and chemical methods for producing zinc silicate (willemite): a review, *Progress in Crystal Growth and characterization of Materials*, 2009, **55**, 98–124.
56. J. l. Brugger, D. McPhail, M. Wallace and J. Waters, Formation of willemite in hydrothermal environments, *Economic Geology*, 2003, **98**, 819–835.
57. D. Medas, F. Podda, C. Meneghini and G. De Giudici, Stability of biological and inorganic hemimorphite: implications for hemimorphite precipitation in non-sulfide Zn deposits, *Ore Geology Reviews*, 2017, **89**, 808–821.
58. S. Pattanaik and F. E. Huggins, Chemical nature of zinc in size fractionated particulate matter from residual oil combustion-A comparative study, *Atmospheric Environment*, 2020, **221**, 117099.
59. T. T. Eighmy, B. S. Crannell, J. E. Krzanowski, L. G. Butler, F. K. Cartledge, E. F. Emery, J. D. Eusden Jr, E. L. Shaw and C. A. Francis, Characterization and phosphate stabilization of dusts from the vitrification of MSW combustion residues, *Waste Management*, 1998, **18**, 513–524.
60. N. Basta, R. Gradwohl, K. Snethen and J. Schroder, Chemical immobilization of lead, zinc, and cadmium in smelter-contaminated soils using biosolids and rock phosphate, *Journal of Environmental Quality*, 2001, **30**, 1222–1230.

61. D. Geysen, C. Vandecasteele, M. Jaspers, E. Brouwers and G. Wauters, Effect of improving flue gas cleaning on characteristics and immobilisation of APC residues from MSW incineration, *Journal of hazardous materials*, 2006, **128**, 27–38.
62. P. Piantone, F. Bodénan, R. Derie and G. Depelsenaire, Monitoring the stabilization of municipal solid waste incineration fly ash by phosphation: mineralogical and balance approach, *Waste Management*, 2003, **23**, 225–243.
63. Y. Tang, H. F. Chappell, M. T. Dove, R. J. Reeder and Y. J. Lee, Zinc incorporation into hydroxylapatite, *Biomaterials*, 2009, **30**, 2864–2872.
64. W. Preis and H. Gamsjäger, Thermodynamic investigation of phase equilibria in metal carbonate–water–carbon dioxide systems, *Monatshefte fuer Chemie/Chemical Monthly*, 2001, **132**, 1327–1346.
65. M. L. D. Gougar, B. E. Scheetz and D. D. Siemer, A novel waste form for disposal of spent-nuclear-fuel reprocessing waste: A vitrifiable cement, *Nuclear technology*, 1999, **125**, 93–103.
66. R. M. Molina, L. A. Schaider, T. C. Donaghey, J. P. Shine and J. D. Brain, Mineralogy affects geoavailability, bioaccessibility and bioavailability of zinc, *Environmental Pollution*, 2013, **182**, 217–224.

View Article Online
DOI: 10.1039/D5EM00651A

Data availability

The data supporting this article have been included in the Supplementary Information.